Earth and Planetary Science Letters 440 (2016) 158–168

Contents lists available at ScienceDirect

Earth and Planetary Science Letters

www.elsevier.com/locate/epsl

Is the mantle chemically stratified? Insights from sound velocity modeling and isotope evolution of an early magma ocean

Eugenia Hyung [a,*], Shichun Huang [b], Michail I. Petaev [a], Stein B. Jacobsen [a]

[a] Department of Earth and Planetary Sciences, Harvard University, 20 Oxford St., Cambridge, MA 02138, USA
[b] Department of Geoscience, University of Nevada, Las Vegas, 4505 S. Maryland Pkwy, Las Vegas, NV 89154, USA

ARTICLE INFO

Article history:
Received 30 October 2015
Received in revised form 29 January 2016
Accepted 1 February 2016
Available online 19 February 2016
Editor: B. Buffett

Keywords:
Fe–Mg partitioning in Al-bearing bridgmanite and ferropericlase
pyrolite lower mantle
layered mantle
magma ocean
terrestrial array

ABSTRACT

The upper mantle is widely accepted to be pyrolitic, but the bulk composition of the lower mantle remains highly disputed. Recent modeling of the lower mantle shear wave velocity profile has suggested that the lower mantle is enriched in bridgmanite, therefore implying a higher Si/Mg than that of the upper mantle. We improve upon such modeling by taking into account Ca-perovskite and considering the distribution of Fe between bridgmanite and ferropericlase, more appropriate for Al-bearing systems. Using available experimental data, we derive a means to constrain Fe–Mg partitioning for bridgmanite and ferropericlase, constrain suitable values for the lower mantle, and apply these to lower mantle shear wave velocity calculations. Calculations that consider the effects of minor chemical components such as Ca and Al suggest that the lower mantle shear wave velocities can resolve PREM for a pyrolitic composition to within 1%. We also model chemical fractionations of the ^{147}Sm–^{143}Nd and ^{176}Lu–^{176}Hf systems induced by a crystallizing magma ocean that would produce a putative Si-enriched lower mantle. The comparison of the calculated $^{143}Nd/^{144}Nd$ and $^{176}Hf/^{177}Hf$ signatures with those of the terrestrial array shows that a Si-enriched lower mantle, if ever formed, no longer exists. Both mineralogical calculations and geochemical magma ocean modeling support the idea that the Earth's lower mantle is likely pyrolitic and that the mantle as a whole need not be chemically stratified.

1. Introduction

The solid Earth is composed of three major chemical layers – the crust, the mantle, and the core. These features were first identified by analyzing seismic waves generated by large-scale earthquakes, penetrating into the interior of the Earth (e.g., Williamson and Adams, 1923). Later, when the physical properties of putative inner Earth materials were measured in high pressure and temperature experiments, inner Earth seismic wave velocities and density profiles were linked to the chemical compositions of these layers (e.g., Birch, 1952).

The silicate mantle is the Earth's volumetrically largest division. Its chemical composition and structure are a constant subject of inquiry and debate as they tie into many issues pertaining to the origin of the Earth and its evolution (e.g., Javoy et al., 2010). One of the most prominent seismic features of the mantle is the 660-km discontinuity, characterized by a sharp jump in seismic velocity. This discontinuity, which serves as the boundary between the upper and lower mantles, has traditionally been attributed to the temperature and pressure-induced breakup of ringwoodite, $(Mg,Fe)_2SiO_4$, into bridgmanite, $(Mg,Fe)SiO_3$ (formerly referred to as "Mg-silicate-perovskite"), and ferropericlase, $(Mg,Fe)O$ (Ito and Takahashi, 1989).

There is yet no consensus on whether this discontinuity is also a chemical boundary (e.g., Irifune et al., 2010; Murakami et al., 2012), which would imply different compositions for the lower and upper mantles. The upper mantle composition is well established from samples of mid-ocean ridge volcanism and mantle peridotites, and is widely presumed to be pyrolitic (McDonough and Sun, 1995). Pyrolite, a theoretical composition calculated as three parts peridotite and one part normal mid-ocean ridge basalt (Ringwood, 1962), is depleted in Si compared to chondrites. Chondrites are often considered to be the building blocks of the Earth. If the bulk Earth has a CI-chondritic Si/Mg ratio, then the compensation for the apparent depletion of Si in the upper mantle is explained either by sequestering of some Si into the core (e.g., Allegre et al., 1995; Georg et al., 2007), or having a higher Si/Mg ratio in the lower mantle (e.g., Taylor and McLennan, 1985), or both.

Such a chemical stratification in the mantle, if it exists, would have most likely been caused by the gravitational settling of dense bridgmanite crystals during the solidification of a magma ocean

* Corresponding author.
E-mail address: hyung@fas.harvard.edu (E. Hyung).

http://dx.doi.org/10.1016/j.epsl.2016.02.001
0012-821X/

not long after the Earth formation (Agee and Walker, 1988). The preservation of such a chemically layered mantle throughout billions of years would imply a lack of material transport between the upper and lower mantles throughout the history of the Earth. Although seismic tomography has revealed slabs penetrating the 660-km discontinuity (Van der Hilst et al., 1997), the extent of material exchange between the upper and lower mantles remains unclear.

The composition of the lower mantle has been evaluated by modeling sound velocity profiles using experimentally derived physical properties of mantle minerals under proper *P–T* conditions (Lee et al., 2004; Stixrude et al., 1992). However, in most experiments, the chemical composition of the lower mantle is approximated by the Fe–Mg–Si–O system, neglecting the less abundant major elements such as Al and Ca. The effect of Al on the shear properties of bridgmanite, having only been explored in the past decade (Jackson, 2004; Murakami et al., 2012), has profound implications for interpreting the lower mantle composition. Using experimental data obtained under lower mantle *P–T* conditions, recent modeled seismic shear wave velocities of a pyrolitic lower mantle (Murakami et al., 2012) were found to have large discrepancies from the shear wave velocities of the 1D seismic profile, PREM (Dziewonski and Anderson, 1981). Specifically, the modeled shear wave velocity profile for a pyrolitic lower mantle with Al-bridgmanite was much lower than PREM (∼3% offset). The difference was resolved by increasing the bridgmanite/ferropericlase ratio in the lower mantle compared to the pyrolitic composition, leading Murakami et al. (2012) to infer a Si-enriched lower mantle.

The approach of Murakami et al. (2012) neglects the contribution of a Ca-bearing phase and the effect of Al on Fe–Mg partitioning between bridgmanite and ferropericlase, which in turn, affects the sound wave speeds of these minerals. Here, we model the shear wave velocities of the lower mantle, taking these effects into account. The pyrolitic mantle contains ∼3–4 wt% CaO (e.g., McDonough and Sun, 1995), which in the lower mantle resides in Ca-perovskite, $CaSiO_3$, occurring alongside two other minerals, bridgmanite and ferropericlase. Although the shear properties of Ca-perovskite have not been measured experimentally, *ab initio* calculations (e.g., Karki and Crain, 1998) of cubic Ca-perovskite have demonstrated high shear velocities which can potentially resolve the discrepancy between a pyrolitic lower mantle and observed seismic wave velocities.

Calculations of lower mantle sound wave velocities usually consider bridgmanite and ferropericlase with Fe–Mg partitioning characteristic of Al-free systems (e.g., Zhang et al., 2013). Al, however, residing exclusively in bridgmanite, affects Fe–Mg partitioning to a substantial degree. Although Al is reported to increase the amount of Fe in bridgmanite due to the coupled substitution of (Fe^{3+} and Al^{3+}) for (Mg^{2+} and Si^{4+}) (Wood and Rubie, 1996), the extreme variability in the data (Fig. 1) has made the subject controversial. In particular, relations among pressure, temperature and Fe–Mg partitioning behavior in coexisting Al-bearing bridgmanite and ferropericlase have so far remained unclear. Another possible complication is the spin transition occurring in ferropericlase, a high pressure effect involving a change in an electron configuration from high spin to low, which subsequently affects both the bulk and shear properties of ferropericlase. As Fe–Mg partitioning between Al-bridgmanite and ferropericlase in the lower mantle can affect shear wave velocity calculations, there is a necessity to critically assess and analyze the available experimental data. Through such an analysis, we present a statistically significant correlation that is capable of predicting K_D values, use this relation to derive K_D suitable for the lower mantle, and apply these to shear wave velocity calculations.

In addition, our study also explores the fractionation of lithophile trace elements in a putative Si-enriched lower mantle that would have formed in a differentiating magma ocean, by taking advantage of primordial fractionation effects in the ^{176}Lu–^{176}Hf and ^{147}Sm–^{143}Nd radiogenic isotope systems between a silicate melt and high-pressure lower mantle phases.

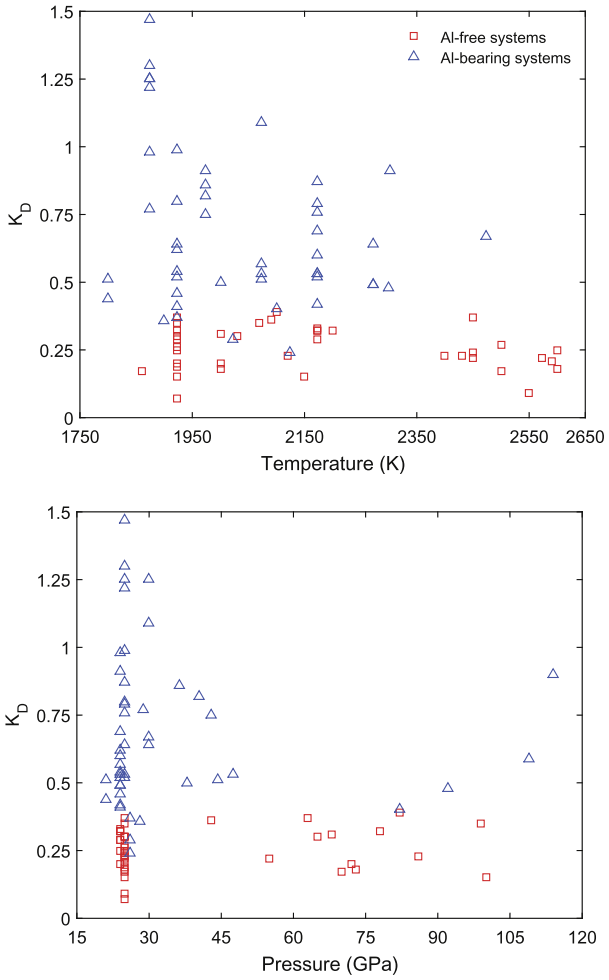

Fig. 1. Variations of K_D values as defined in Eq. (5), with temperature and pressure. Blue, upward-pointing triangles and red squares denote data for Al-bearing (Frost and Langenhorst, 2002; Irifune et al., 2010; McCammon et al., 2004; Murakami, 2005; Nishiyama and Yagi, 2003; Sinmyo and Hirose, 2013; Wood and Rubie, 1996; Wood, 2000) and Al-free systems (Auzende et al., 2008; Frost and Langenhorst, 2002; Nakajima et al., 2012; Sakai et al., 2009), respectively. (For interpretation of the references to color in this figure legend, the reader is referred to the web version of this article.)

Using approaches from mineral physics and geochemistry, we evaluate the likelihood of a chemically stratified mantle, with the lower mantle being enriched in Si compared to the upper mantle.

2. Methods

2.1. Shear wave velocity modeling

Modeling a seismic velocity profile of a planetary layer such as the lower mantle involves a series of calculations for different depths of the layer. Each step calculates the compound shear wave velocities for a mineral aggregate representing a bulk chemical composition at a given pressure and temperature. For the calculations of the aggregate shear wave velocity of a pyrolitic lower mantle, the mineral proportions of lower mantle minerals (∼77.5 vol% bridgmanite [Al–$(Mg, Fe)SiO_3$]–15 vol% ferropericlase [$(Mg, Fe)O$], and ∼7.5 vol% Ca-perovskite [$CaSiO_3$]) (e.g., Irifune, 1994) are used. Since the amount of Fe in ferropericlase or bridgmanite affects the wt% proportions of these minerals, we consider minor variations in the volume and weight proportions of lower

Table 1
Elastic constants used in shear wave velocity calculations.

Parameter	Bridgmanite	Ca-pv	Ferropericlase	
			high spin	low spin
ρ_0 (g/cm^3)	set to vary*	4.23 (Ricolleau et al., 2009)	set to vary*	set to vary*
K_{T0} (GPa)	267.6(9) (Andrault et al., 2007; Fiquet et al., 2000)	244 (Ricolleau et al., 2009)	158 (Ricolleau et al., 2009) (fixed)	170 (Ricolleau et al., 2009) (fixed)
K'_0	3.78(3) (Fiquet et al., 2000)	4†	4†	4†
G_0 (GPa)	164(2) (Murakami et al., 2012)	165 (Karki and Crain, 1998)	varies*‡	varies*‡
G'_0	1.71(2)‡	2.46 (Karki and Crain, 1998)	varies*‡	varies*‡
α_0 (K^{-1})	2.2×10^{-5} (Funamori et al., 1996)	2.2×10^{-5} (Shim and Duffy, 2000)	3.15×10^{-5} (Dubrovinsky and Saxena, 1997)	
γ_0	1.48 (Stixrude and Lithgow-Bertelloni, 2005)	1.53 (Shim and Duffy, 2000)	1.5 (Stixrude and Lithgow-Bertelloni, 2005)	
$(\partial G/\partial T)$ (GPa K^{-1})	−0.020(1) (Murakami et al., 2012)	−0.023(6) (Cammarano et al., 2003)	−0.020(1) (Murakami et al., 2012)	

* Set to vary as a function of iron content. Density of bridgmanite: $\rho_0 = 4.11 + 0.01 \times (100–\text{Mg\#})$ g/cm^3.
Density of ferropericlase: calculated assuming $V_0 = 11.24$ cm^3 mol^{-1} for pure MgO (Smyth and McCormick, 1995) for both spin states, where V_0 is the volume at zero pressure.
† Fixed. See e.g., Ricolleau et al. (2009).
‡ G values are adapted from Jacobsen et al. (2002) for the high spin state of ferropericlase, and from Murakami et al. (2012) for the low spin states of ferropericlase, which each vary as a function of iron content. Suitable G' values for the third-order Eulerian finite strain equation are rederived by either performing a least squares fitting of existing data to the formulation of Stixrude and Lithgow-Bertelloni (2005) where available, or fitting synthetic data that was generated by applying G and G' values to the second-order Eulerian finite strain equation (Davies and Dziewonski, 1975). All other elastic constants were chosen from the literature.

mantle minerals corresponding to different K_D values, to account for small volume and density changes that Fe inflicts for each corresponding phase. The lower mantle Fe/(Fe + Mg) is set to 0.107 (McDonough and Sun, 1995), similar to earlier estimates by Green et al. (1979) and Jagoutz et al. (1979).

For the calculation of the shear wave velocity profile of the lower mantle, we utilize the third-order Eulerian finite-strain equation (Stixrude and Lithgow-Bertelloni, 2005) to calculate shear modulus (G), where the non-thermal portion is expressed as follows:

$$G = (1+2f)^{5/2}\left[G_0 + \left(3K_{S0}G'_0 - 5G_0\right)f + \left(6K_{S0}G'_0 - 24K_{S0} - 14G_0 + 9/2K_{S0}K'_0\right)f^2\right]. \quad (1)$$

Here, G_0 is the shear modulus at zero pressure, G'_0 is the pressure derivative of the shear modulus, K_0, the bulk modulus, and K'_0, the pressure derivative of the bulk modulus. This expression is thermodynamically self-consistent to f^2, where f, the finite strain, is defined as:

$$f = \frac{1}{2}\left[\left(\frac{\rho}{\rho_0}\right)^{\frac{2}{3}} - 1\right] \quad (2)$$

where ρ is density at corresponding depth, and ρ_0 is the density at zero pressure. K_{S0} is the isentropic bulk modulus at zero pressure:

$$K_{S0} = K_{T0}(1 + \alpha_0\gamma_0 T). \quad (3)$$

Here, T is the temperature at ambient pressure; K_{T0}, the isothermal bulk modulus; α_0, the thermal expansion coefficient; and γ_0, the Grüneisen parameter. Temperature corrections for shear modulus are made using linear projections (e.g., Deschamps and Trampert, 2004). We adopted the Voigt–Reuss Hill averaging method (Hill, 1952) for the aggregate shear modulus of Mg-perovskite, ferropericlase, and Ca-perovskite of the lower mantle. For the aggregate density of the lower mantle in calculating shear wave velocity, PREM (Dziewonski and Anderson, 1981) is used. Model calculations are performed along an adiabatic geotherm (Brown and Shankland, 1981).

For the shear properties (G, G') of bridgmanite, we use experimentally derived values from Murakami et al. (2012), which were used to argue for a Si-enriched lower mantle. The Fe-content in bridgmanite has been experimentally shown to have no bearing on its shear modulus (Chantel et al., 2012). In contrast, the shear properties of ferropericlase are affected by Fe. When calculating the change in the shear properties of ferropericlase with respect to its Fe/Mg ratio, we refer to the studies of Jacobsen et al. (2002) and Murakami et al. (2012). The pressure derivatives of the shear modulus (G') in the original experiments are derived using the second order Eulerian finite-strain equation (Davies and Dziewonski, 1975). For internal consistency in calculations, G' is re-derived using the third order expansion of the Eulerian finite strain equation (Stixrude and Lithgow-Bertelloni, 2005) by refitting the raw data if reported, or refitting synthetic data generated using the published elastic constants as described in the footnote of Table 1. As there are no experimental data on the shear properties of Ca-perovskite, following Matas et al. (2007), we use *ab initio* calculations of Karki and Crain (1998).

2.2. Deriving K_D: finding a correlation between different chemical components

The partitioning of Mg and Fe between bridgmanite (pv) and ferropericlase (fp) in Al-free systems is described by the following reaction:

$$\text{MgSiO}_3(\text{pv}) + \text{FeO}(\text{fp}) \leftrightarrow \text{FeSiO}_3(\text{pv}) + \text{MgO}(\text{fp}) \quad (4)$$

where the partition coefficient, K_D, expresses the distribution of Fe and Mg end-member components between the two coexisting phases:

$$K_D = \left(X^{\text{pv}}_{\text{Fe}}/X^{\text{pv}}_{\text{Mg}}\right)/\left(X^{\text{fp}}_{\text{Fe}}/X^{\text{fp}}_{\text{Mg}}\right). \quad (5)$$

Here, X^a_i is the mole fraction of component i in phase a. Typical K_D values in the Fe–Mg–Si–O systems range from 0.2 to 0.3 (Auzende et al., 2008; Kobayashi et al., 2005; Mao et al., 1997; Sakai et al., 2009), implying higher molar Fe/Mg ratios in ferropericlase than in bridgmanite. In Al-bearing systems however, K_D values are higher by a factor of two or more and show large variations (Fig. 1). This phenomenon is largely attributed to the coupled substitution of (Fe^{3+} + Al^{3+}) for (Mg^{2+} + Si^{4+}) in bridgmanite,

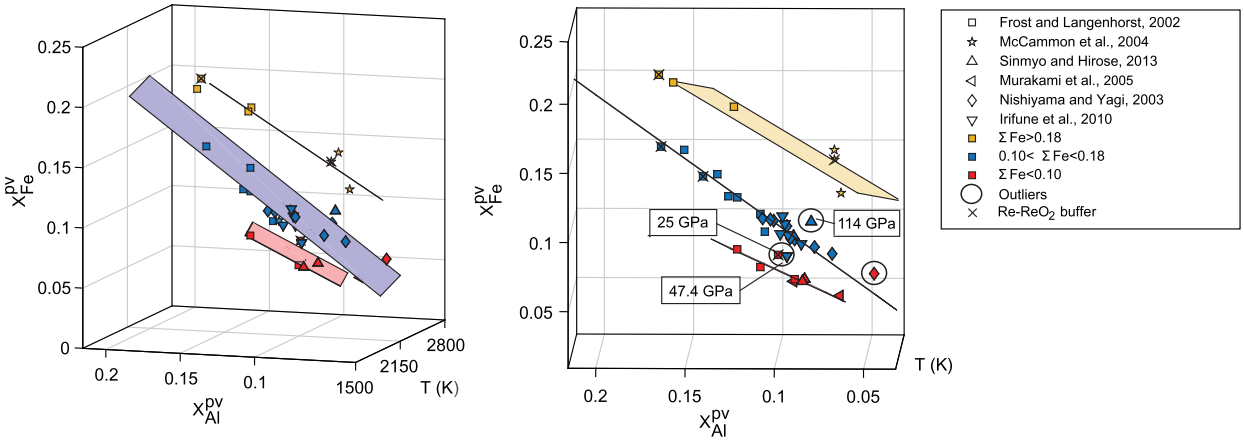

Fig. 2. The relationship between X_{Fe}^{pv}, X_{Al}^{pv}, and T in Al-bearing systems. The mole fractions are in apfu units, while T is in K. The same plot is shown from two different angles for clarity. The data form three planar clusters roughly corresponding to the bulk Fe# of the system: the yellow plane corresponds to Fe#>0.18, the blue plane to an Fe# of <0.10–0.18 which is inclusive of the bulk silicate Earth, and the red plane to Fe#<0.10. The data sources are indicated in the legend. To avoid cluttering, only the most oxidizing experiments buffered by Re–ReO_2 (2 log units above QFM) are marked by crosses. Other experimental data were acquired at more reducing conditions spanning from the CO_2–CO buffer (2 log units below QFM) to the IW buffer (~3.5 log units below QFM), provided the equilibration of the experimental charge with Fe capsules has been achieved. (For interpretation of the references to color in this figure legend, the reader is referred to the web version of this article.)

where Fe^{3+} is thought to reside preferentially in the dodecahedral (A) site, and Al^{3+} in the octahedral (B) site in the form of $(Mg^{2+}, Fe^{2+}, Fe^{3+})(Al^{3+}, Si^{4+})O_3$ (Wood and Rubie, 1996). From the stoichiometric considerations alone, contents of Fe^{3+} measured by Mossbauer spectroscopy or EELS (electron energy-loss spectroscopy) imply a "spill over" of Al^{3+} to the dodecahedral site in the form of $(Mg^{2+}, Fe^{2+}, Fe^{3+}, Al^{3+})(Al^{3+}, Si^{4+})O_3$, and in some cases, an additional "spill over" of Fe^{3+} from the dodecahedral to the octahedral site as $(Mg^{2+}, Fe^{2+}, Fe^{3+}, Al^{3+})(Al^{3+}, Fe^{3+}, Si^{4+})O_3$. As literature data typically do not separate Fe^{3+} and Fe^{2+} when reporting K_D, an apparent K_D (K_{Dapp}) is often reported instead, where $X_{Fe}^{pv} = (Fe^{2+} + Fe^{3+})/(Fe^{2+} + Fe^{3+} + Mg)$. For the sake of simplicity, hereafter we refer to K_{Dapp} as K_D.

We examine the correlations between different chemical components and experimental conditions for the purpose of deriving a relationship or model that may be capable of predicting K_D values applicable to the lower mantle. In such an assessment of K_D for Al-bearing systems, different chemical components, Al content in bridgmanite (X_{Al}^{pv}) in atoms per formula unit (apfu), Fe-content ($Fe^{2+} + Fe^{3+}$) in bridgmanite in apfu (X_{Fe}^{pv}), and Fe-content in ferropericlase in apfu (X_{Fe}^{fp}), as well as experimental temperature (K) and pressure (GPa) are compiled from a number of literature sources and treated as variables. The apfu values are directly quoted from studies, or calculated from the reported mineral analyses when necessary (Frost and Langenhorst, 2002; Irifune et al., 2010; McCammon et al., 2004; Murakami, 2005; Nishiyama and Yagi, 2003; Sinmyo and Hirose, 2013).

Plotting different chemical components in 3D Cartesian coordinates (X_{Fe}^{fp} *vs* X_{Fe}^{pv} *vs* X_{Fe}^{pv}) reveals three groups of data, arranged qualitatively by the bulk Fe/(Fe + Mg) ratio (Fe# hereafter) of the bridgmanite-ferropericlase system. These data groups – labeled "low," "middle," and "high" hereafter – roughly correspond to the bulk Fe# of below 0.10, 0.10–0.18, and higher than 0.18, respectively. The "middle" data group that includes the pyrolitic composition (~0.107) also contains the highest abundance of data, and therefore was deemed best suited for statistical analysis. This data group was used to derive a model correlation among different chemical components and experimental conditions. Experimental temperatures in this group typically range from 1800 to 2400 K, spanning the range of the lower mantle, while pressures range from 24 to 114 GPa. Coefficients of each of the independent components (any combination of T, P, X_{Fe}^{fp}, X_{Al}^{pv}, X_{Fe}^{pv}, K_D) were derived in relation to one component that was treated as a dependent variable (any of T, P, X_{Fe}^{fp}, X_{Al}^{pv}, X_{Fe}^{pv}) through linear least squares fitting, in the form of:

$$y = a_1x_1 + a_2x_2 + \cdots + a_nx_n + \cdots + b. \quad (6)$$

Here, y is the dependent variable, x_1 to x_n are independent variables, a_1 to a_n are the coefficients of the independent variables, and b is a constant. Correlations where X_i^a was potentially both a dependent and independent variable (e.g., $K_D = aX_{Fe}^{pv} + b$) were avoided in such an approach, as there would be little to no predictive value. The statistical likelihood of a correlation between randomly selected chemical components and experimental conditions was then assessed by calculating p-values as a test of statistical significance for the coefficients of independent variables simultaneously. Here the null hypothesis is an absence of a correlation between the dependent and independent variables. Following convention, p-values were deemed to indicate statistical significance at a value of 0.05 or less. A correlation was rejected as statistically insignificant and thus unlikely when p-values were higher than 0.05 for any coefficient, including the constant.

Components with a high probability of being related to one another were plotted in Cartesian coordinates (Fig. 2) to visually assess the linear least squares fitting. Here the criterion for assessing the quality of the data was more rigorous. Each individual data point that was noted to deviate from the trend was assessed, and deemed to be an outlier when its inclusion to the data set caused the p-value of a coefficient to surpass 0.01. For the sake of completeness, we also plotted the experimental data that failed the p-test and were excluded from calculating regression coefficients. The derived relation was further used to calculate K_D values (Section 3.2).

2.3. Magma ocean modeling

It is widely believed that the interior of the early Earth once contained a partially or completely molten reservoir of silicate material referred to as a magma ocean (e.g., Elkins-Tanton, 2012). If such a magma ocean was deep enough to include a large, or the entire portion of the lower mantle, then the fractionation of Mg and Si, and thus Si-enrichment in the lower mantle would have most likely been generated during early magma ocean crystallization accompanied by gravitational settling of bridgmanite. The enrichment of the lower mantle in bridgmanite would, in turn, fractionate lithophile trace elements such as Lu, Hf, Sm, and Nd,

leaving the upper mantle enriched in some elements and depleted in others. This is because bridgmanite and Ca-perovskite are either greatly depleted or enriched in Sm, Nd, and Lu relative to the melt from which they crystallize (Table 3).

Consequentially, a comparison of modeled trace element patterns produced by a putative bridgmanite settling with available trace element signatures of the upper mantle can shed light on whether this feature is still present if it has ever occurred. We test the hypothesis of a layered mantle through a simplified magma ocean model that explores trace element fractionation in such a scenario. Although the solidification of a magma ocean is expected to produce increasingly denser materials from bottom up due to progressive enrichment of residual liquid in FeO (e.g., Elkins-Tanton et al., 2003), we do not consider this effect in our model, because likely gravitational instability and overturn would erase any features of large scale mantle layering. For comparison of our model with the data, we refer to the Hf–Nd signatures of accessible mantle samples, commonly known as the terrestrial array (hereafter denoted as the terrestrial Hf–Nd array, to avoid confusion with the "mantle array") (Vervoort et al., 2011, 1999). The dataset currently contains $^{176}Hf/^{177}Hf$ and $^{143}Nd/^{144}Nd$ ratios of more than 3500 samples from the continental and oceanic crust, and the depleted mantle. These ratios are often expressed in ε-units (ε_{Hf} or ε_{Nd}), which are defined as the isotopic ratio deviations from those of chondrites, or CHUR (the CHondritic Uniform Reservoir), in parts per 10,000.

Following Albarede et al. (2000) and Caro et al. (2005), we assume a magma ocean with chondritic Sm/Nd and Lu/Hf ratios generated by an event such as the Moon-forming giant impact (e.g., Tonks and Melosh, 1993). Although Boyet and Carlson (2005) argued for a superchondritic Sm/Nd ratio of the bulk Earth based on the silicate Earth $^{142}Nd/^{144}Nd$ ratios being about 20 ppm higher than in ordinary chondrites, Huang et al. (2013) showed that the long-lived ^{147}Sm–^{143}Nd isotopic systematics are inconsistent with a superchondritic Sm/Nd ratio for the silicate Earth. A superchondritic Sm/Nd ratio for bulk Earth inferred from the extinct ^{146}Sm–^{142}Nd depends on two assumptions: (i) the bulk Earth is isotopically most similar to ordinary chondrites and (ii) the difference between ordinary chondrites and the Earth results from radioactive decay of ^{146}Sm in a silicate Earth with a higher than ordinary chondrite Sm/Nd ratio. As discussed by Huang et al. (2013) it is not clear whether any of these assumptions are correct. First, the bulk Earth is isotopically more similar to enstatite chondrites than ordinary chondrites. Second, the available ^{147}Sm–^{143}Nd isotopic data for terrestrial rocks do not support a superchondritic Sm/Nd ratio for the Earth. Clearly, there are too many uncertainties in how to use the extinct ^{146}Sm–^{142}Nd isotopic system for the type of modeling done for the long-lived ^{147}Sm–^{143}Nd and ^{176}Lu–^{176}Hf isotopic systems. For this reason, we do not discuss the issue of a possible superchondritic Sm/Nd ratio further in this paper.

Upon cooling, the magma ocean crystallized bridgmanite and Ca-perovskite. It is unlikely that the Earth evolved from a single magma ocean; however, we assume one for the purposes of testing the hypothesis of a homogeneously Si-enriched lower mantle forming during magma ocean crystallization as suggested by Murakami et al. (2012). We neglect ferropericlase because its trace element fractionation effects are negligible compared to bridgmanite and Ca-perovskite (e.g., Walter et al., 2004).

Although the timing of such a large-scale differentiation event(s) is unclear, the last magma ocean forming event is thought to have been the Moon-forming giant impact, with the estimated timing of this event of about 30 Ma (Jacobsen, 2005) but not exceeding 100 Ma (Yu and Jacobsen, 2011) after the formation of the first Solar System condensates at 4.567 Ga. Here we assume the onset of upper and lower mantle differentiation to occur at 4.467 Ga.

Because Ca-perovskite has the largest effect on the solid–melt partitioning of Sm, Nd, and Lu, and because the crystallization sequence of Ca-perovskite in relation to bridgmanite is unclear, we varied its amount in Si-enriched lower mantle scenarios, ranging from 2 wt% Ca-perovskite (+98 wt% bridgmanite) to 7 wt% Ca-perovskite (+93 wt% bridgmanite), with 1 wt% increments. The calculated model signatures of the upper mantle are plotted in ε-units along with their complementary lower mantle compositions. Here the upper mantle is set to take up 27 wt% of the whole mantle.

We consider two end-member magma ocean crystallization scenarios representing batch (or equilibrium) and fractional crystallization (subscripts "eq" and "fr", respectively) using equations from Caro et al. (2005) modified to include the effects of radioactive decay. Described below is the case for the Sm–Nd system, which equally applies to the Lu–Hf system when considering Lu in place of Sm, and Hf in place of Nd.

The bulk solid–liquid partition coefficient, D, is defined as:

$$D_E = \sum_m D_E^m \alpha^m \tag{7}$$

where α^m is the mass fraction of mineral m, and D_E^m represents the crystal/melt partition coefficient of element E in mineral m.

First, the upper mantle $^{147}Sm/^{144}Nd$ ratio (R^{UM}) is calculated after assuming complete solidification of the lower mantle:

$$R_{eq}^{UM} = \left(^{147}Sm/^{144}Nd\right)_{CHUR}\left[\frac{(1-F)(D_{Nd}-1)+1}{(1-F)(D_{Sm}-1)+1}\right] \tag{8}$$

$$R_{fr}^{UM} = \left(^{147}Sm/^{144}Nd\right)_{CHUR}\left(\frac{F^{D_{Sm}-1}}{F^{D_{Nd}-1}}\right) \tag{9}$$

where $1-F$ is the weight fraction of the lower mantle compared to the whole mantle, and F is the melt fraction (upper mantle).

The complementary lower mantle $^{147}Sm/^{144}Nd$ ratios (R^{LM}) for the two crystallization models were calculated as follows:

$$R_{eq}^{LM} = \left(^{147}Sm/^{144}Nd\right)_{CHUR}\left(\frac{D_{Sm}}{D_{Nd}}\right)\left[\frac{(1-F)(D_{Nd}-1)+1}{(1-F)(D_{Sm}-1)+1}\right] \tag{10}$$

$$R_{fr}^{LM} = \left(^{147}Sm/^{144}Nd\right)_{CHUR}\left(\frac{1-F^{D_{Sm}}}{1-F^{D_{Nd}}}\right). \tag{11}$$

The evolution of the $^{143}Nd/^{144}Nd$ ratio before and after magma ocean crystallization is modeled using standard radioactive decay equations. For example, for the upper mantle we have:

$$\begin{aligned} &^{143}Nd/^{144}Nd_{eq(UM)} \\ &= {}^{143}Nd/^{144}Nd_{CHUR(today)} - {}^{147}Sm/^{144}Nd_{CHUR(today)}\left(e^{\lambda t_E}-1\right) \\ &\quad + {}^{147}Sm/^{144}Nd_{CHUR(today)}\left(e^{\lambda t_E}-e^{\lambda t}\right) + R_{eq}^{UM}{}_{(today)}\left(e^{\lambda t}-1\right) \end{aligned} \tag{12}$$

where t_E is the age of the Earth, and t is the time passed from magma ocean crystallization to present, and λ, the decay constant of the radioactive parent isotope. Expressions are analogous for the Lu–Hf system.

The solid–melt partition coefficients and CHUR values used in the modeling are listed in Tables 2 and 3, respectively.

3. Results and discussion

3.1. A statistically significant relationship between chemical components and temperature for Al-bridgmanite

The statistical treatment of experimental data on bridgmanite equilibrated with ferropericlase reveals a correlation in each data

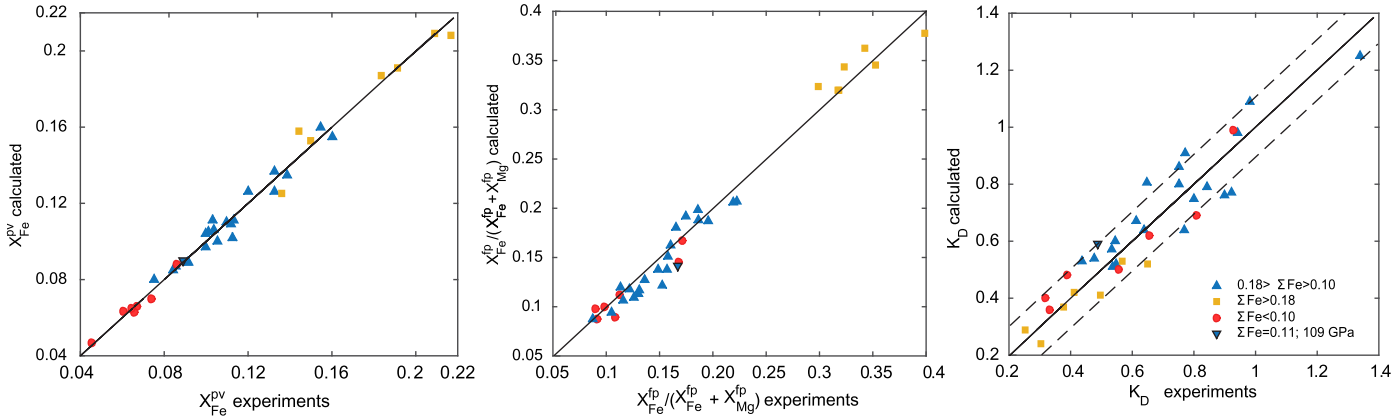

Fig. 3. Reproducibility of X^{pv}_{Fe} (left), $X^{fp}_{Fe}/(X^{fp}_{Fe}+X^{fp}_{Mg})$ (middle) and K_D (right) calculated with Eqs. (13)–(15). The dashed lines in the right-most plot delineate a ±0.10 uncertainty band. $R^2 = 0.87$ for all data. The reproducibility of the experimental K_D value at 109 GPa (downward-pointing triangle) implies that K_D is unlikely to be significantly (>0.10) affected by the spin transition of ferropericlase. Data that are deemed outliers in Fig. 2 are not included in the plots.

Table 2
Solid–melt partition coefficients used in modeling.

	Sm	Nd	Lu	Hf
Bridgmanite	0.050(2)[1]	0.0161(4)[1]	1.00(2)[2]	1.64(5)[2]
Ca-perovskite	21.1(10)[1]	16.7(10)[1]	13.5(7)[1]	1.70(2)[1]

Here the solid–melt partition coefficients of ferropericlase are assumed to be negligible. The numbers in parentheses next to the partition coefficients in the table indicate uncertainty.
[1] Corgne et al. (2005).
[2] Walter et al. (2004).

Table 3
Present day CHUR values for magma ocean modeling.

Ratios	$^{147}Sm/^{144}Nd$	$^{143}Nd/^{144}Nd$	$^{176}Lu/^{177}Hf$	$^{176}Hf/^{177}Hf$
Values	0.1967[1]	0.512638[1]	0.0336[2]	0.282785[2]

[1] Jacobsen and Wasserburg (1984).
[2] Bouvier et al. (2008).

group which relates the Al-content in bridgmanite, the Fe-content in bridgmanite, and temperature (K):

$$aX^{pv}_{Fe} + bT + cX^{pv}_{Al} + d = 0. \quad (13)$$

Such a formulation naturally forms a plane in 3-dimensional coordinates, whose axes represent X^{pv}_{Fe} *vs* X^{pv}_{Al} *vs* T (Fig. 2). Pressure as a variable (ranging from 24 to 109 GPa) was found to be statistically insignificant (p-value >0.6) and thus excluded in relation to other components in Eq. (13). All of the components presented in Fig. 2 are directly quoted from the literature or calculated from reported chemical analyses, with no additional treatment to the data.

For the "middle" group (Fig. 2; blue), the trend is well-defined. The coefficients of the linear least squares fitting are $a = 1.26$, $b = 3.36 \times 10^{-5}$, $c = -1$, and $d = -0.0978$. When X^{pv}_{Al} is treated as the dependent variable, the p-value of coefficient b (the temperature component) is $\sim 1 \times 10^{-3}$ for the data compiled for this range of bulk Fe# when excluding outliers, whereas the p-value of coefficient a (component X^{pv}_{Fe}) is closer to 10^{-11}.

P-values for the coefficients of X^{pv}_{Fe} in relation to X^{pv}_{Al} for the "low" and "high" groups of data are similarly low, on the order of 10^{-6}. On the other hand, the p-values for the coefficients of the temperature component in the "high" and "low" groups are ~0.06 and ~0.15 respectively, possibly due to a weaker correlation compared to the relationship between X^{pv}_{Al} *vs* X^{pv}_{Fe}, or more likely due to the small data set. Although the "low" and "high" data groups are not directly applicable to the bulk silicate Earth (BSE), they do give important insights into crystal chemistry of bridgmanite as discussed in Section 3.2.

3.2. K_D for Al-bearing systems

The correlations between bridgmanite composition and temperature (Eq. (13)) in all three groups with different Fe# imply that the derived trends may be controlled by the crystal chemistry of Al-bearing bridgmanite. It appears that there is a correlation between the Fe# of a group and how Al^{3+} and Fe^{3+} are distributed between different sites. In the "high" group (Fig. 2, yellow), the Fe^{3+}/Al^{3+} ratio is close to 1 within 1 sigma uncertainty of X^{pv}_{Fe} and $Fe^{3+}/\Sigma Fe$ measurements (Frost and Langenhorst, 2002; McCammon et al., 2004), requiring, by a charge balance, Al^{3+} and Fe^{3+} to occupy the octahedral and dodecahedral sites, respectively. In the "low" group (Fig. 2, red) the Al^{3+}/Fe^{3+} ratio exceeds 1.5 (Frost and Langenhorst, 2002), requiring Al^{3+} to occupy both the octahedral and dodecahedral sites, leading to a chemical formula of $(Mg^{2+}, Fe^{2+}, Fe^{3+}, Al^{3+})(Al^{3+}, Si^{4+})O_3$. The latter also applies to the "middle" group which exhibits a slight overabundance of Al^{3+} compared to Fe^{3+} (Al^{3+}/Fe^{3+} ~1.2; Frost and Langenhorst, 2002). Clearly, there is a positive correlation between the bulk Fe# and the amount of Fe^{3+} in the system that would be expected at constant redox conditions expressed as, say, the Fe^{3+}/Fe^{2+} ratio. However, experiments conducted under different controlled redox conditions span at least 6 log units of fO_2 (Fig. 2), hence leaving the reason for such a correlation between the bulk Fe# and Fe^{3+}/Fe^{2+} ratio unclear.

Although the definition of K_D requires the knowledge of the Fe/Mg ratios of both bridgmanite and ferropericlase, as Eq. (13) only constrains the Fe-content of bridgmanite, the amount of Fe in ferropericlase is inferred indirectly. Using Eq. (13) to constrain the Fe-content in Al-bearing bridgmanite, the Fe/Mg ratio of bridgmanite is approximated as:

$$X^{pv}_{Fe}/X^{pv}_{Mg} = X^{pv}_{Fe}/(1 - X^{pv}_{Fe}). \quad (14)$$

Then the X^{fp}_{Fe} of ferropericlase is calculated from the mass balances of Fe and Mg:

$$eX^{pv}_{Fe}/(X^{pv}_{Fe} + X^{pv}_{Mg}) + fX^{fp}_{Fe}/(X^{fp}_{Fe} + X^{fp}_{Mg}) = Fe\# \quad (15)$$

where e and f are the respective mineral proportions of bridgmanite and ferropericlase in the experimental charge. For pyrolitic compositions, e and f are 0.685 and 0.315.

The calculated Fe-contents in Al-bridgmanite, and ferropericlase (Eqs. (13)–(15)) as well as corresponding K_D values reproduce the experimental data very well (Fig. 3). Despite potential errors

associated with approximations of the Fe/Mg ratio in bridgmanite (Eq. (14)) and the indirect inference of X_{Fe}^{fp} (Eq. (15)), 75% of the calculated K_D values plot within ±0.10 of the experimental values, while 90% of the calculated K_D values plot within ±0.15 ($R^2 = 0.87$).

The effect of the bulk Fe# on the K_D is well demonstrated by two experiments conducted at the same pressure of 24 GPa, near similar X_{Al}^{pv} of 0.107 and 0.103, similar temperatures of 1923 and 1873 K, but different bulk Fe# of 0.133 and 0.110 by Frost and Langenhorst (2002) and Nishiyama and Yagi (2003), respectively. Although the expected response from a conventional exchange equilibrium reaction dictates that the K_D values should be similar for the same intensive parameters despite different bulk compositions, the experiment at higher Fe# yields K_D of 0.46, while at lower Fe# the K_D is 0.98. Our set of equations that takes into account the bulk Fe# reproduces such a behavior very well (Fig. 3, right).

Our finding that the Fe–Mg partitioning between Al-bearing bridgmanite and ferropericlase is strongly controlled by bridgmanite questions the notion (e.g., Irifune et al., 2010) that Fe-partitioning behavior in Al-bearing systems is affected by the spin transition of Fe in ferropericlase. For instance, a substantial decrease (of ~0.3) in K_D at 44 GPa compared to lower pressure values in the study of Irifune et al. (2010) can be explained by the difference in the Al content of bridgmanite, with $X_{Al}^{pv} = 0.087$ apfu and $X_{Al}^{pv} \geq 0.094$, at high and lower pressures, respectively. Here, the decrease in K_D is a reflection of the high sensitivity of K_D to Al-content in bridgmanite rather than due to the spin transition in ferropericlase. Moreover, the 47 GPa data point (Irifune et al., 2010) plots very close to a low pressure (25 GPa) data of Frost and Langenhorst (2002) (circled; Fig. 2). The reason for the deviations of these points from the determined trends in 3D space is unclear. In contrast, a data point at 109 GPa (Sinmyo and Hirose, 2013) is shown to conform to trends in Fig. 2, where the calculated K_D value reproduces the experimental value to within 0.10 (Fig. 3). This further suggests that observed variations in K_D values are typically not related to the high pressure (>60 GPa) effects involving the spin transition in ferropericlase.

Although the large variation in K_D for Al-bearing systems (Fig. 1) was attributed to the possible lack of equilibrium across experiments (e.g., Frost and Langenhorst, 2002), we find the quality of the data to be more or less consistent from study to study. This is based on the observation that the data follow distinct trends, which are largely defined by experimental conditions such as temperature and the charge composition rather than by lab (study) and/or apparatus type (diamond anvil *vs* multi-anvil cell).

3.3. Calculation of lower mantle seismic profiles when considering Ca-perovskite and K_D

The lower mantle shear wave velocity profile of the mixture of bridgmanite and ferropericlase in pyrolitic proportions (8:2 in volume) using the K_D value of 0.24, typical of Al-free systems, yields a maximum offset from PREM of 3.3%, consistent with the calculations of Murakami et al. (2012). The addition of Ca-perovskite to the mixture while still assuming a K_D of 0.24 reduces the offset of the calculations from PREM to around 1.6%, with the offset normalized to PREM at a maximum at lower pressures (<60 GPa).

However, the primitive mantle composition contains 4.5 wt% Al_2O_3 (McDonough and Sun, 1995), which mostly resides in bridgmanite (~5 wt% Al_2O_3). For the bulk silicate Earth Fe# of 0.107, the solution of Eq. (13)–(15) yields a K_D value of ~1.05 at 1880 K, corresponding to a depth of 670 km (24 GPa) in the lower mantle. K_D decreases along the lower mantle adiabatic temperature profile (Brown and Shankland, 1981) to ~0.65 near 125 GPa (Fig. 4, top).

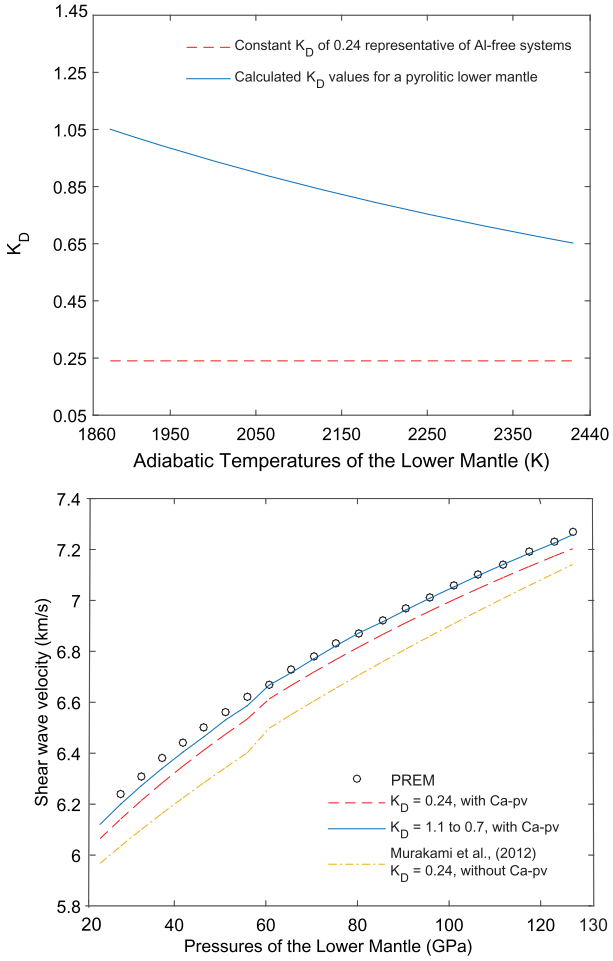

Fig. 4. Variations of K_D (top) and shear wave velocity (bottom) along the lower mantle adiabatic geotherm. Top: Calculation of projected K_D values of the lower mantle based on analysis of experimental data on an adiabatic geotherm. The blue solid line shows K_D values for a pyrolitic lower mantle (McDonough and Sun, 1995). The dashed red line ($K_D = 0.24$) is characteristic of Al-free systems. Note that the change of K_D with mantle depth is due to the temperature change along an adiabatic geotherm, independent of corresponding pressure change. There is no significant effect assumed from the spin transition in ferropericlase (see text for details). Bottom: Open circles – PREM, yellow dash–dotted line – the model of Murakami et al. (2012) with constant $K_D = 0.24$ and no Ca-perovskite (Ca-pv), red dashed line – $K_D = 0.24$ with Ca-perovskite, solid blue line – variable K_D plus Ca-perovskite. The consideration of Ca-perovskite and high K_D values characteristic of an Al-bearing pyrolitic model allows for the pyrolitic lower mantle composition to match PREM to within 1%. (For interpretation of the references to color in this figure legend, the reader is referred to the web version of this article.)

Increasing K_D from 0.24 to higher values characteristic of the BSE diminishes the discrepancy of lower mantle shear wave velocity calculations from PREM to 0.2–0.6%. Meanwhile, considerations in the 1 sigma uncertainties in the thermoelastic constants of Al-bridgmanite alone in these calculations yields an uncertainty in lower mantle shear wave velocity calculations of ~±1%. An uncertainty of ±0.10 in K_D values translates to a ~±0.1% uncertainty in shear wave velocity calculations, which is negligible in comparison.

The changes in shear and bulk properties induced by the spin transition of Fe in ferropericlase are noticeable in pyrolitic lower mantle shear wave velocity calculations as a small jump at ~60 GPa, whereas such features are not apparent in seismic 1D shear wave velocity models. The velocity jump from high spin to low spin at 60 GPa (~1500 km depth from the Earth's surface) is calculated to be 0.3%. In contrast, variations in shear wave velocities in 3D tomographic models such as S40RTS (Ritsema et al., 2011), reveal shear wave velocity anomalies of up to ±1.5%, with

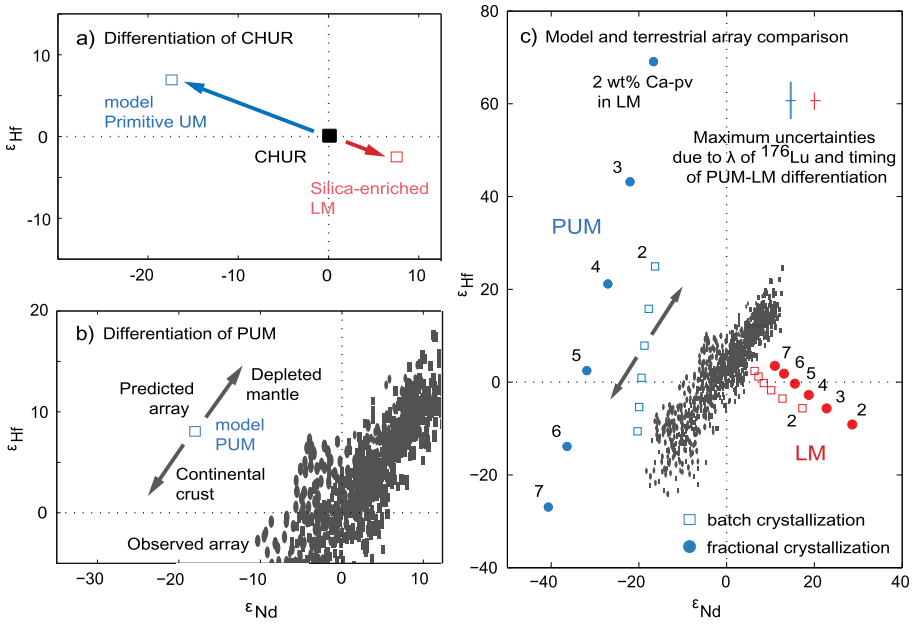

Fig. 5. The effect of putative Si-enriched lower mantle on the Hf–Nd signatures of the upper mantle: Model *vs* Observations. The blue and red symbols represent the putative primitive upper (PUM) and complementary Si-enriched lower mantles, respectively. Open squares and filled circles denote batch and fractional crystallization models, respectively. (a) A cartoon illustrating how the compositions of the model upper (blue arrow) and lower (red arrow) mantle would evolve during crystallization of the CHUR magma ocean at 4.467 Ga. (b) A cartoon illustrating how the ε_{Hf} and ε_{Nd} of putative upper mantle would fractionate (grey arrows) as it differentiates into a depleted upper mantle (DUM) and the crust. The grey symbols show the present day terrestrial Hf–Nd array (Vervoort et al., 2011, 1999). (c) Model results. This model uses the decay constants of 1.867×10^{-11} yr^{-1} for ^{176}Lu (Söderlund et al., 2004), and 6.54×10^{-9} yr^{-1} for ^{147}Sm (Kossert et al., 2009). The numbered blue and red symbols show respectively the compositions of the putative upper and lower mantles at different contents of Ca-perovskite (Ca-pv, numbers next to the symbols) in the modeled Si-enriched lower mantle. The grey symbols show the terrestrial Hf–Nd array. The red and blue crosses in the upper right corner show maximum uncertainties induced by the different values of ^{176}Lu decay constant and the timing of the mantle differentiation, respectively. The lack of overlap between the modeled PUM reservoirs complementary to a putative Si-enriched lower mantle and the terrestrial array argues against the presence of a Si-enriched lower mantle in the present Earth. (For interpretation of the references to color in this figure legend, the reader is referred to the web version of this article.)

no clear indication of a global velocity change occurring at depths corresponding to range ~60 GPa. It may well be that seismic 1D models are incapable of resolving such a small scale discontinuity as one expected around 60 GPa, as inferred from tomographic shear wave velocity variations that are much larger than the change of velocity incurred by the spin transition of Fe in ferropericlase at such depths. Alternatively, an absence of a feature in 1D seismic models may be explained by a gradual spin transition over a range of pressures in the mantle as observed in experiments (e.g., Badro, 2014), rather than by an abrupt change at around 60 GPa.

The calculations in this study demonstrate the importance of less abundant major elements such as Ca and Al in modeling shear wave velocities of the lower mantle. We note that the large offset of the shear wave velocity calculations of a pyrolitic lower mantle, demonstrated to be incompatible with PREM by up to 3.2% (Murakami et al., 2012), can be resolved by considering Ca-perovskite and Fe–Mg partitioning values characteristic of Al-bearing lower mantle minerals. As Ca and Al cannot be excluded from the bulk silicate Earth, the considerations of a Ca-bearing phase and the effects of Al on the shear wave velocity model of the lower mantle support a lower mantle of a pyrolitic composition over one that is Si-enriched.

3.4. Trace element signatures of magma ocean crystallization

Kato et al. (1988) have previously explored possible trace element fractionation during the solidification of a terrestrial magma ocean to conclude that the mantle was unlikely to be chemically stratified. Owing to recent claims of a chemically stratified mantle involving the entire volume of the lower mantle, here we explore the fractionation of trace elements due to the formation of a Si-enriched lower mantle using the Hf–Nd isotopic systems, while comparing the results to the terrestrial array. Such a test is limited to the layered mantle scenario because only the lack of communication between the upper and lower mantles would have been capable of preserving these signatures.

The gravitational settling of denser crystals during the magma ocean crystallization results in an enrichment of the lower mantle in Si compared to both the chondritic source and the complementary residual melt, which formed the upper mantle. Once the crystallization front rises to a depth where the bridgmanite and Ca-perovskite become unstable, substantial fractionation of trace elements is no longer possible. At this point the silicate magma ocean consists of 73 wt% solids, corresponding to the weight proportion of the silicate lower mantle, and 27 wt% residual melt which later solidifies to form the primitive, pyrolitic upper mantle ("PUM"; Fig. 5a). Subsequent repeated remelting of the Earth throughout its geologic history produces materials of the terrestrial Hf–Nd array representing the continental and ocean crust, as well as the depleted mantle (Blichert-Toft and Albarede, 1997; Vervoort et al., 2011, 1999).

The differentiation of the bulk silicate Earth into the model PUM and Si-enriched lower mantle results in a strong fractionation trend in ε_{Hf}–ε_{Nd} space (Fig. 5). The model PUM is enriched in Nd relative to CHUR in all variants of lower mantle model compo-

sitions explored here, exhibiting negative ε values. The Sm and Hf content of the upper mantle, on the other hand, are strongly controlled by the assumed Ca-perovskite content in the lower mantle. The ε_{Hf}–ε_{Nd} signatures of the upper and lower mantles fractionate up to dozens of ε-units away from the CHUR in opposite, but complementary directions. The subsequent differentiation of the PUM (arrows in Fig. 5b) into the depleted mantle and crust is anticipated to transform a single PUM ε_{Hf}–ε_{Nd} value (blue points in Fig. 5c) into an array with a slope parallel to that of the terrestrial Hf–Nd array.

The consequences of having a Si-enriched lower mantle formed in a large-scale differentiation event are demonstrated in Fig. 5c by the modeled ε_{Hf} and ε_{Nd} signatures of the upper and lower mantles. Despite wide variations in Ca-perovskite content, the fractionation of the trace elements is so large, that none of the modeled PUM ε_{Hf}–ε_{Nd} values comes close to CHUR, or remotely overlaps with the PUM fractionation line of the present day terrestrial Hf–Nd array.

As the D values for the of the Sm–Nd and Lu–Hf isotope systems used here are measured at pressures close to the 660-km discontinuity, it is possible that the partition coefficients may change with pressure and temperature. In such a case, D values may well increase with increasing pressure because of a positive Clapeyron-slope of fusion in silicates (Liebske et al., 2005). This would tend to increase the fractionation effects of the ε_{Hf}–ε_{Nd} signatures (Fig. 5c), making the difference between modeled ε_{Hf}–ε_{Nd} signatures and the terrestrial Hf–Nd array larger.

The timing of differentiation of a global magma ocean and the uncertainty in the ^{176}Lu decay constant are also incapable of significantly affecting large fractionation effects predicted by a model with a Si-enriched lower mantle. The ε_{Hf} values are affected by the different plausible values of the ^{176}Lu decay constant (Bizzarro et al., 2003; Scherer et al., 2001) by about 1 ε-unit at most. The explored difference in the onset of mantle differentiation by $\pm$100 Ma results in a maximum shift of the ε_{Hf}–ε_{Nd} values by $\pm$2 ε-units. None of these factors compensates for the lack of overlap between our model upper mantle ε_{Hf} and ε_{Nd} values and the terrestrial Hf–Nd array.

We note that the PUM ε_{Hf}–ε_{Nd} signatures resulting from the formation of a Si-enriched lower mantle (Fig. 5c) cannot be erased by subsequent upper mantle melting, as these ε_{Hf}–ε_{Nd} signatures are strongly controlled by minerals that are stable only under lower mantle conditions. Therefore, the lack of overlap between our model and the terrestrial Hf–Nd array makes a Si-enriched lower mantle containing more than 93 wt% bridgmanite at present day unlikely. In contrast, an early decoupling of Hf–Nd signatures (e.g., Puchtel et al., 2013) suggests that chemical layering was present early on, although often inferred to occur at depths well into the lower mantle. Even if there was once chemical stratification in the mantle involving a composition change at the 660-km discontinuity, the upper and lower mantles have been subsequently disturbed and remixed rather than preserved perhaps during vigorous convection predicted by models of magma ocean evolution (Tonks and Melosh, 1993).

4. Conclusions

The shear-wave velocity model of the lower mantle matches the pyrolitic composition to within 1% when the contribution of Ca-perovskite and relatively high K_D values characteristic of Al-bearing systems are taken into account.

The evaluation of experimental data on Fe–Mg partitioning between bridgmanite and ferropericlase in Al-bearing systems shows that K_D depends upon the Al content, the bulk Fe# of the system, and temperature. Dependence of K_D on pressure up to 109 GPa is not significant. K_D is also unlikely to be substantially ($>$0.10) affected by the spin transition of Fe in ferropericlase. For the bulk silicate Earth composition combined with lower mantle temperature conditions, K_D values likely exceed 0.65 throughout the whole lower mantle, approaching $\sim$1.05 near the 660-km discontinuity.

Our modeling of the crystallization of a magma ocean with a Si-enriched lower mantle yields ε_{Hf} and ε_{Nd} signatures that do not overlap with the present day terrestrial array, implying that if such a Si-enriched lower mantle has ever formed, it was not preserved throughout Earth's history. It may be concluded that the lower mantle is likely pyrolitic, and that the mantle as a whole need not be chemically stratified.

Acknowledgements

This work was financially supported by the NSF Graduate Research Fellowship (EH), NASA cosmochemistry grant NNX12AH65G (SBJ), and NSF grant EAR1144727 (SBJ and SH). We thank S. Park and P. Bogiatzis for helpful discussions in the subject of seismology, I. Jackson and I. S. Puchtel for journal reviews, and B. Buffett for editorial handling. SH acknowledges support by NSF grant EAR-1524387.

Appendix A. Supplementary material

Supplementary material related to this article can be found online at http://dx.doi.org/10.1016/j.epsl.2016.02.001.

References

Agee, C., Walker, D., 1988. Mass balance and phase density constraints on early differentiation of chondritic mantle. Earth Planet. Sci. Lett. 90, 144–156.
Albarede, F., Blichert-Toft, J., Vervoort, J., Gleason, J., Rosing, M., 2000. Hf–Nd isotope evidence for a transient dynamic regime in the early terrestrial mantle. Nature 404, 488–490.
Allegre, C.J., Poirier, J., Humler, E., Hofmann, A.W., 1995. The chemical composition of the Earth. Earth Planet. Sci. Lett. 134, 515–526.
Andrault, D., Bolfan-Casanova, N., Bouhifd, M.A., Guignot, N., Kawamoto, T., 2007. The role of Al-defects on the equation of state of Al–(Mg,Fe)SiO_3 perovskite. Earth Planet. Sci. Lett. 263, 167–179. http://dx.doi.org/10.1016/j.epsl.2007.08.012.
Auzende, A.-L., Badro, J., Ryerson, F.J., Weber, P.K., Fallon, S.J., Addad, A., Siebert, J., Fiquet, G., 2008. Element partitioning between magnesium silicate perovskite and ferropericlase: new insights into bulk lower-mantle geochemistry. Earth Planet. Sci. Lett. 269, 164–174. http://dx.doi.org/10.1016/j.epsl.2008.02.001.
Badro, J., 2014. Spin transitions in mantle minerals. Annu. Rev. Earth Planet. Sci. 42, 231–248. http://dx.doi.org/10.1146/annurev-earth-042711-105304.
Birch, F., 1952. Elasticity and consitution of the Earth's interior. J. Geophys. Res. 57, 227–286.
Bizzarro, M., Baker, J.A., Haack, H., Ulfbeck, D., Rosing, M., 2003. Early history of Earth's crust–mantle system inferred from hafnium isotopes in chondrites. Nature 421, 931–933. http://dx.doi.org/10.1038/nature01421.
Blichert-Toft, J., Albarede, F., 1997. The Lu–Hf isotope geochemistry of chondrites and the evolution of the mantle–crust system. Earth Planet. Sci. Lett. 148, 243–258.
Bouvier, A., Vervoort, J.D., Patchett, P.J., 2008. The Lu–Hf and Sm–Nd isotopic composition of CHUR: constraints from unequilibrated chondrites and implications for the bulk composition of terrestrial planets. Earth Planet. Sci. Lett. 273, 48–57. http://dx.doi.org/10.1016/j.epsl.2008.06.010.
Boyet, M., Carlson, R.W., 2005. ^{142}Nd evidence for early (>4.53 Ga) global differentiation of the silicate Earth. Science 80 (309), 576–581. http://dx.doi.org/10.1126/science.1113634.
Brown, J.M., Shankland, T.J., 1981. Thermodynamic parameters in the Earth as determined from seismic profiles. Geophys. J. R. Astron. Soc. 66, 579–596.
Cammarano, F., Goes, S., Vacher, P., Giardini, D., 2003. Inferring upper-mantle temperatures from seismic velocities. Phys. Earth Planet. Inter. 138, 197–222. http://dx.doi.org/10.1016/S0031-9201(03)00156-0.
Caro, G., Bourdon, B., Wood, B.J., Corgne, A., 2005. Trace-element fractionation in Hadean mantle generated by melt segregation from a magma ocean. Nature 436, 246–249. http://dx.doi.org/10.1038/nature03827.
Chantel, J., Frost, D.J., McCammon, C.A., Jing, Z., Wang, Y., 2012. Acoustic velocities of pure and iron-bearing magnesium silicate perovskite measured to 25 GPa and 1200 K. Geophys. Res. Lett. 39, L19307. http://dx.doi.org/10.1029/2012GL053075.
Corgne, A., Liebske, C., Wood, B.J., Rubie, D.C., Frost, D.J., 2005. Silicate perovskite-melt partitioning of trace elements and geochemical signature of a deep perovskitic reservoir. Geochim. Cosmochim. Acta 69, 485–496. http://dx.doi.org/10.1016/j.gca.2004.06.041.

Davies, G.F., Dziewonski, A., 1975. Homogeneity and constitution of the Earth's lower mantle and outer core. Phys. Earth Planet. Inter. 10, 336–343.

Deschamps, F., Trampert, J., 2004. Towards a lower mantle reference temperature and composition. Earth Planet. Sci. Lett. 222, 161–175. http://dx.doi.org/10.1016/j.epsl.2004.02.024.

Dubrovinsky, L.S., Saxena, S.K., 1997. Thermal expansion of periclase (MgO) and tungsten (W) to melting temperatures. Phys. Chem. Miner. 24, 547–550. http://dx.doi.org/10.1007/s002690050070.

Dziewonski, A., Anderson, D.L., 1981. Preliminary reference Earth model. Phys. Earth Planet. Inter. 25, 297–356.

Elkins-Tanton, L.T., 2012. Magma oceans in the inner solar system. Annu. Rev. Earth Planet. Sci. 40, 113–139. http://dx.doi.org/10.1146/annurev-earth-042711-105503.

Elkins-Tanton, L.T., Parmentier, E.M., Hess, P.C., 2003. Magma ocean fractional crystallization and cumulate overturn in terrestrial planets: implications for Mars. Meteorit. Planet. Sci. 38, 1753–1771. http://dx.doi.org/10.1111/j.1945-5100.2003.tb00013.x.

Fiquet, G., Dewaele, A., Andrault, D., Kunz, M., Le Bihan, T., 2000. Thermoelastic properties and crystal structure of MgSiO perovskite at lower mantle pressure and temperature conditions. Geophys. Res. Lett. 27, 21–24.

Frost, D.J., Langenhorst, F., 2002. The effect of Al_2O_3 on Fe–Mg partitioning between magnesiowustite and magnesium silicate perovskite. Earth Planet. Sci. Lett. 199, 227–241.

Funamori, N., Yagi, T., Utsumi, W., Kondo, T., Uchida, T., 1996. Thermoelastic properties of $MgSiO_3$ perovskite determined by in situ X ray observations up to 30 GPa and 2000 K. J. Geophys. Res. 101, 8257–8269.

Georg, R.B., Halliday, A.N., Schauble, E.A., Reynolds, B.C., 2007. Silicon in the Earth's core. Nature 447, 1102–1106. http://dx.doi.org/10.1038/nature05927.

Green, D.H., Hibberson, W.O., Jaques, A.L., 1979. Petrogenesis of mid-ocean ridge basalts. In: McElhinny, M.W. (Ed.), The Earth: Its Origin, Structure and Evolution. Academic Press, London, pp. 265–299.

Hill, R., 1952. The elastic behaviour of a crystalline aggregate. Proc. Phys. Soc. 65, 349–354.

Huang, S., Jacobsen, S.B., Mukhopadhyay, S., 2013. ^{147}Sm–^{143}Nd systematics of Earth are inconsistent with a superchondritic Sm/Nd ratio. Proc. Natl. Acad. Sci. USA 110, 4929–4934. http://dx.doi.org/10.1073/pnas.1222252110.

Irifune, T., 1994. Absence of an aluminous phase in the upper part of the Earth's lower mantle. Nature 370, 131–133.

Irifune, T., Shinmei, T., Mccammon, C.A., Miyajima, N., Rubie, D.C., Frost, D.J., 2010. Iron partitioning and density changes of pyrolite in Earth's lower mantle. Science 1, 193–195.

Ito, E., Takahashi, E., 1989. Postspinel transformations in the system Mg_2SiO_4–Fe_2SiO_4 and some geophysical implications. J. Geophys. Res. 94, 10,637–10,646.

Jackson, J.M., 2004. Sound velocities and elasticity of aluminous $MgSiO_3$ perovskite: implications for aluminum heterogeneity in Earth's lower mantle. Geophys. Res. Lett. 31, L10614. http://dx.doi.org/10.1029/2004GL019918.

Jacobsen, S.B., 2005. The Hf–W isotopic system and the origin of the Earth and Moon. Annu. Rev. Earth Planet. Sci. 33, 531–570. http://dx.doi.org/10.1146/annurev.earth.33.092203.122614.

Jacobsen, S.B., Wasserburg, G.J., 1984. Sm–Nd isotopic evolution of chondrites and achondrites, II. Earth Planet. Sci. Lett. 67, 137–150.

Jacobsen, S.D., Reichmann, H., Spetzler, H.A., Mackwell, S.J., Smyth, J.R., Angel, R.J., Mccammon, C.A., 2002. Structure and elasticity of single-crystal (Mg, Fe)O and a new method of generating shear waves for gigahertz ultrasonic interferometry. J. Geophys. Res. 107, 2037–2050.

Jagoutz, E., Palme, H., Baddenhausen, H., Blum, K., Cendales, M., Dreibus, G., Spettel, B., Lorenz, V., Wanke, H., 1979. The abundances of major, minor and trace elements in the earth's mantle as derived from primitive ultramafic nodules. In: Proc. Lunar Planet. Sci. Conf. 10th, pp. 2031–2050.

Javoy, M., Kaminski, E., Guyot, F., Andrault, D., Sanloup, C., Moreira, M., Labrosse, S., Jambon, A., Agrinier, P., Davaille, A., Jaupart, C., 2010. The chemical composition of the Earth: enstatite chondrite models. Earth Planet. Sci. Lett. 293, 259–268. http://dx.doi.org/10.1016/j.epsl.2010.02.033.

Karki, B.B., Crain, J., 1998. First principles determination of elastic properties of $CaSiO_3$ perovskite at lower mantle pressures. Geophys. Res. Lett. 25, 2741–2744.

Kato, T., Ringwood, A.E., Irifune, T., 1988. Experimental determination of element partitioning between silicate perovskites, garnets and liquids: constraints on early differentiation of the mantle. Earth Planet. Sci. Lett. 89, 123–145.

Kobayashi, Y., Kondo, T., Ohtani, E., Hirao, N., Miyajima, N., Yagi, T., Nagase, T., Kikegawa, T., 2005. Fe–Mg partitioning between $(Mg,Fe)SiO_3$ post-perovskite, perovskite, and magnesiowüstite in the Earth's lower mantle. Geophys. Res. Lett. 32. http://dx.doi.org/10.1029/2005GL023257.

Kossert, K., Jörg, G., Nähle, O., v. Gostomski, C.L., 2009. High-precision measurement of the half-life of ^{147}Sm. Appl. Radiat. Isot. 67, 1702–1706.

Lee, K.K.M., O'Neill, B., Panero, W.R., Shim, S.-H., Benedetti, L.R., Jeanloz, R., 2004. Equations of state of the high-pressure phases of a natural peridotite and implications for the Earth's lower mantle. Earth Planet. Sci. Lett. 223, 381–393. http://dx.doi.org/10.1016/j.epsl.2004.04.033.

Liebske, C., Corgne, A., Frost, D.J., Rubie, D.C., Wood, B.J., 2005. Compositional effects on element partitioning between Mg-silicate perovskite and silicate melts. Contrib. Mineral. Petrol. 149, 113–128. http://dx.doi.org/10.1007/s00410-004-0641-8.

Mao, H., Shen, G., Hemley, R., 1997. Multivariable dependence of Fe–Mg partitioning in the lower mantle. Science 278, 2098–2100.

Matas, J., Bass, J., Ricard, Y., Mattern, E., Bukowinski, M.S.T., 2007. On the bulk composition of the lower mantle: predictions and limitations from generalized inversion of radial seismic profiles. Geophys. J. Int. 170, 764–780.

McCammon, C.A., Lauterbach, S., Seifert, F., Langenhorst, F., van Aken, P.A., 2004. Iron oxidation state in lower mantle mineral assemblages. Earth Planet. Sci. Lett. 222, 435–449. http://dx.doi.org/10.1016/j.epsl.2004.03.018.

McDonough, W., Sun, S.-s., 1995. The composition of the Earth. Chem. Geol. 120, 223–253. http://dx.doi.org/10.1016/0009-2541(94)00140-4.

Murakami, M., 2005. Post-perovskite phase transition and mineral chemistry in the pyrolitic lowermost mantle. Geophys. Res. Lett. 32, L03304. http://dx.doi.org/10.1029/2004GL021956.

Murakami, M., Ohishi, Y., Hirao, N., Hirose, K., 2012. A perovskitic lower mantle inferred from high-pressure, high-temperature sound velocity data. Nature 485, 90–94. http://dx.doi.org/10.1038/nature11004.

Nakajima, Y., Frost, D.J., Rubie, D.C., 2012. Ferrous iron partitioning between magnesium silicate perovskite and ferropericlase and the composition of perovskite in the Earth's lower mantle. J. Geophys. Res. 117, B08201. http://dx.doi.org/10.1029/2012JB009151.

Nishiyama, N., Yagi, T., 2003. Phase relation and mineral chemistry in pyrolite to 2200 °C under the lower mantle pressures and implications for dynamics of mantle plumes. J. Geophys. Res. 108, 2255. http://dx.doi.org/10.1029/2002JB002216.

Puchtel, I.S., Blichert-Toft, J., Touboul, M., Walker, R.J., Byerly, G.R., Nisbet, E.G., Anhaeusser, C.R., 2013. Insights into early Earth from Barberton komatiites: evidence from lithophile isotope and trace element systematics. Geochim. Cosmochim. Acta 108, 63–90. http://dx.doi.org/10.1016/j.gca.2013.01.016.

Ricolleau, A., Fei, Y., Cottrell, E., Watson, H., 2009. Density profile of pyrolite under the lower mantle conditions. Geophys. Res. Lett. 36, L06302. http://dx.doi.org/10.1029/2008GL036759.

Ringwood, A.E., 1962. A model for the upper mantle. J. Geophys. Res. 67, 857–867.

Ritsema, J., Deuss, A., Van Heijst, H.J., Woodhouse, J.H., 2011. S40RTS: a degree-40 shear-velocity model for the mantle from new Rayleigh wave dispersion, teleseismic traveltime and normal-mode splitting function measurements. Geophys. J. Int. 184, 1223–1236. http://dx.doi.org/10.1111/j.1365-246X.2010.04884.x.

Sakai, T., Ohtani, E., Terasaki, H., Sawada, N., Kobayashi, Y., Miyahara, M., Nishijima, M., Hirao, N., Ohishi, Y., Kikegawa, T., 2009. Fe–Mg partitioning between perovskite and ferropericlase in the lower mantle. Am. Mineral. 94, 921–925. http://dx.doi.org/10.2138/am.2009.3123.

Scherer, E., Munker, C., Mezger, K., 2001. Calibration of the lutetium–hafnium clock. Science 293, 683–687. http://dx.doi.org/10.1126/science.1061372.

Shim, S.-H., Duffy, T.S., 2000. The stability and P–V–T equation of state of $CaSiO_3$ perovskite in the Earth's lower mantle. J. Geophys. Res. 105 (25), 25955–25968.

Sinmyo, R., Hirose, K., 2013. Iron partitioning in pyrolitic lower mantle. Phys. Chem. Miner. 40, 107–113. http://dx.doi.org/10.1007/s00269-012-0551-7.

Smyth, J.R., McCormick, T.C., 1995. Crystallographic data for minerals. In: Ahrens, T.J. (Ed.), Mineral Physics and Crystallography: A Handbook of Physical Constants. American Geophysical Union, Washington D.C., pp. 1–17.

Söderlund, U., Patchett, P.J., Vervoort, J.D., Isachsen, C.E., 2004. The ^{176}Lu decay constant determined by Lu–Hf and U–Pb isotope systematics of Precambrian mafic intrusions. Earth Planet. Sci. Lett. 219, 311–324. http://dx.doi.org/10.1016/S0012-821X(04)00012-3.

Stixrude, L., Hemley, R.J., Fei, Y., Mao, H.K., 1992. Thermoelasticity of silicate perovskite and magnesiowüstite and stratification of the Earth's mantle. Science 257, 1099–1101.

Stixrude, L., Lithgow-Bertelloni, C., 2005. Thermodynamics of mantle minerals – I. Physical properties. Geophys. J. Int. 162, 610–632. http://dx.doi.org/10.1111/j.1365-246X.2005.02642.x.

Taylor, S.R., McLennan, S.M., 1985. The continental crust: its composition and evolution. In: Hallan, A. (Ed.), The Continental Crust: Its Composition and Evolution. Blackwell Publishing Ltd, Oxford, pp. 256–276.

Tonks, W.B., Melosh, H.J., 1993. Magma ocean formation due to giant impacts. J. Geophys. Res. 98, 5319–5333.

Van der Hilst, R.D., Widyantoro, S., Engdahl, E.R., 1997. Evidence for deep mantle circulation from global tomography. Nature 386, 578–584.

Vervoort, J.D., Patchett, P.J., Blichert-Toft, J., Albarede, F., 1999. Relationships between Lu–Hf and Sm–Nd isotopic systems in the global sedimentary system. Earth Planet. Sci. Lett. 168, 79–99.

Vervoort, J.D., Plank, T., Prytulak, J., 2011. The Hf–Nd isotopic composition of marine sediments. Geochim. Cosmochim. Acta 75, 5903–5926. http://dx.doi.org/10.1016/j.gca.2011.07.046.

Walter, M.J., Nakamura, E., Trønnes, R.G., Frost, D.J., 2004. Experimental constraints on crystallization differentiation in a deep magma ocean. Geochim. Cosmochim. Acta 68, 4267–4284. http://dx.doi.org/10.1016/j.gca.2004.03.014.

Williamson, E.D., Adams, L.H., 1923. Density of the Earth. J. Wash. Acad. Sci. 13, 413–414.

Wood, B.J., 2000. Phase transformations and partitioning relations in peridotite under lower mantle conditions. Earth Planet. Sci. Lett. 174, 341–354.

Wood, B.J., Rubie, D.C., 1996. The effect of alumina on phase transformations at the 660-kilometer discontinuity from Fe–Mg partitioning experiments. Science 80 (273), 1522–1524.

Yu, G., Jacobsen, S.B., 2011. Fast accretion of the Earth with a late Moon-forming giant impact. Proc. Natl. Acad. Sci. USA 108. http://dx.doi.org/10.1073/pnas.1108544108.

Zhang, Z., Stixrude, L., Brodholt, J., 2013. Elastic properties of $MgSiO_3$-perovskite under lower mantle conditions and the composition of the deep Earth. Earth Planet. Sci. Lett. 379, 1–12. http://dx.doi.org/10.1016/j.epsl.2013.07.034.